

1 **Measurement Report: Elevated excess-NH₃ can**
2 **promote the redox reaction to produce HONO:**
3 **Insights from the COVID-19 pandemic**

4 Xinyuan Zhang^{1,2}, Lingling Wang³, Nan Wang³, Shuangliang Ma³, Shenbo
5 Wang^{2,4} *, Ruiqin Zhang^{2,4**}, Dong Zhang^{1,2}, Mingkai Wang^{2,4}, Hongyu
6 Zhang^{1,2}.

7
8 ¹ College of Chemistry, Zhengzhou University, Zhengzhou, 450000, China

9 ² Research Institute of Environmental Sciences, Zhengzhou University, Zhengzhou
10 450000, China

11 ³ Henan Provincial Ecological Environment Monitoring and Safety Center, Zhengzhou,
12 450000, China

13 ⁴ School of Ecology and Environment, Zhengzhou University, Zhengzhou, 450000,
14 China

15

16 **Correspondence:** Shenbo Wang (shbwang@zzu.edu.cn) and Ruiqin Zhang
17 (rqzhang@zzu.edu.cn)

18

19 **Abstract**

20 HONO plays a crucial role as a precursor to OH radicals in the tropospheric atmosphere.

21 The incongruity between HONO concentration and NO_x emissions during the COVID-

22 19 pandemic remains puzzling. Here, we show evidence from field observations of ten

23 sites in China that there was a noticeable increase in NH₃ concentrations during the

24 COVID-19 pandemic. In addition to the meteorological conditions, the significant

25 decrease in sulfate and nitrate concentrations enhanced the portioning of NH₄⁺ to NH₃.

26 Such conditions enable enhanced particle pH values, which in turn accelerate the redox

27 reactions between NO₂ and SO₂ to form HONO. This mechanism partly explains the

28 lower reduction of HONO concentration than that of NO₂ concentration during the

29 pandemic and highlights the importance of coordinating the control of SO₂, NO_x, and

30 NH₃ emissions.

31 **Keywords:** Ammonia, HONO, Gas-particle portioning, Acidity, COVID-19 pandemic

32

33 **1. Introduction**

34 Nitrous acid (HONO) is a critical precursor of hydroxyl radical (OH), contributing
35 to more than 60% of OH production (Alicke, 2003; Platt et al., 1980; Kleffmann et al.,
36 2005). The OH can react with carbon monoxide, nitrogen oxides (NO_x), sulfur dioxide
37 (SO₂), and volatile organic compounds to produce secondary pollutants such as ozone
38 (O₃) and PM_{2.5} (particulate matter with an aerodynamic diameter less than or equal to
39 2.5 μm), thereby affecting air quality, human health, and global climate change (Li et
40 al., 2021a; Wang et al., 2023b; Lu et al., 2018)

41 High concentrations of HONO are present in urban daytime atmospheres, and
42 exploring its sources has become a hot and challenging topic in the field of atmospheric
43 chemistry (Jiang et al., 2022; Xu et al., 2019). Various sources of atmospheric HONO
44 have been identified, including combustion processes (e.g., vehicle emissions) (Kramer
45 et al., 2020; Liao et al., 2021; Li et al., 2021b), direct emissions from soil (Su and Zhang,
46 2011; Oswald et al., 2013; Meusel et al., 2018), homogeneous reactions between NO
47 and OH radicals (Pagsberg et al., 1997; Atkinson et al., 2004), heterogeneous reactions
48 of NO₂ on aerosols and ground surfaces (Zhang et al., 2020a; McFall et al., 2018; Liu
49 et al., 2014, 2020a), and photolysis of nitrate (Spataro and Ianniello, 2014; Scharko et
50 al., 2014; Romer et al., 2018; Ye et al., 2017; Shi et al., 2021). During the pandemic
51 control periods, there was a substantial reduction in vehicle traffic flow and industrial
52 emissions, leading to a decrease of more than 60% in NO_x emissions in eastern China
53 (Huang et al., 2021a). It was initially expected that the concentration of HONO would
54 also decrease proportionally. However, Liu et al. (2020b) observed that the decrease in

55 HONO concentration during the pandemic period was only 31%, which was
56 significantly lower than the reductions in NO (62%) and NO₂ (36%). Furthermore, the
57 observed concentrations of HONO during the COVID-19 pandemic in 2020 were
58 higher than those during the corresponding period in 2021 in Beijing (Luo et al., 2023).
59 These findings suggest the existence of a considerable unknown source of HONO
60 during the COVID-19 pandemic period.

61 Ammonia (NH₃) is a primary alkaline gas in the atmosphere, capable of influencing
62 the pH level of particulate matter and plays a crucial role in the atmospheric nitrogen
63 cycle (Gu et al., 2022; Xu et al., 2020; Gong et al., 2011). Several studies have indicated
64 that NH₃ can promote the formation of HONO by promoting the hydrolysis of NO₂ (Xu
65 et al., 2019) or the redox reaction of NO₂ with SO₂ (Liu et al., 2023). Moreover,
66 previous studies have reported that NH₃ concentrations in the atmosphere, particularly
67 in rural areas, significantly increased during the pandemic (Xu et al., 2022; Cui, 2023;
68 Zhang et al., 2020b). Consequently, the rise in NH₃ may contribute to the enhanced
69 formation of HONO (Huang et al., 2021a). Unfortunately, there is currently a lack of
70 research on the relationship between enhanced NH₃ and HONO during the COVID-19
71 pandemic period.

72 To address this, online observational data on the chemical composition of PM_{2.5},
73 gaseous pollutants, and meteorological conditions at ten sites in China before and
74 during the COVID-19 pandemic period were analyzed to investigate the variation in
75 NH₃ concentrations and particle pH, and explore the promoting effect of increased pH
76 values on HONO formation.

77 **2. Materials and methods**

78 **2.1 Observation sites**

79 Online measurements were conducted at four urban and six rural sites in Henan
80 Province, China from January 1 to February 29, 2020, including Sanmenxia (U-SMX),
81 Zhoukou (U-ZK), Zhumadian (U-ZMD), and Xinyang (U-XY), as well as rural
82 locations including Anyang (R-AY), Xinxiang (R-XX), Jiaozuo (R-JZ), Shangqiu (R-
83 SQ), Nanyang (R-NY), and Puyang (R-PY). Descriptions and the spatial distribution
84 of these ten sites can be found in Table S1 and Fig. S1.

85 **2.2 Measurements**

86 The aerosol and gas monitor (MARGA, Metrohm, Switzerland) was used to analyze
87 the hourly water-soluble ions (Na^+ , NH_4^+ , K^+ , Mg^{2+} , Ca^{2+} , Cl^- , NO_3^- , and SO_4^{2-}) in $\text{PM}_{2.5}$,
88 as well as gaseous species (NH_3 , HNO_3 , HCl , and HONO) at ten sampling sites. The
89 MARGA instrument is widely used (Chen et al., 2017; Stieger et al., 2019; Twigg et al.,
90 2022). A detailed description of the instrument and QA/QC can be found in Text S1. In
91 brief, the atmospheric sample passes through a $\text{PM}_{2.5}$ cut-off head, and both particles
92 and gases enter a wet rotating dissolution device for diffusion. Subsequently, the
93 particles in the sample undergo hygroscopic growth and condensation in an aerosol
94 supersaturated vapor generator, followed by collection and ion chromatographic
95 analysis. The gases in the sample are oxidized by H_2O_2 in the dissolution device,
96 absorbed into a liquid solvent, and then entered the gas sample collection chamber for

97 ion chromatographic quantification. The range of minimum detection limits for water-
98 soluble ions was between 0.002 $\mu\text{g}/\text{m}^3$ (Cl^-) to 0.081 $\mu\text{g}/\text{m}^3$ (NH_4^+). Uncertainties of 20%
99 are assumed for the detection of NH_3 and NH_4^+ , while uncertainties of 10% are assumed
100 for other components (Wang et al., 2020, 2022a). **In addition, a detailed description of**
101 **HONO measurement using this system can be found in Text S2.** Overall, the limit of
102 detection for HONO was 4 pptv and the uncertainty was estimated to be $\pm 20\%$.

103 The data for NO_2 and SO_2 were obtained from a series of instruments provided by
104 Thermo Fisher Scientific (USA). The hourly concentrations of organic carbon (OC) in
105 $\text{PM}_{2.5}$ were analyzed using a carbon analyzer (Model 4, Sunset Laboratory., USA).
106 Detailed descriptions of the NO_2 , SO_2 , and carbon analyzers can be found in Text S3.
107 The smart weather stations (LUFFTWS500, Sutron, Germany) were utilized for
108 synchronized observation of meteorological parameters including pressure,
109 temperature (T), and relative humidity (RH).

110 **2.3 Data analysis.**

111 **2.3.1 pH prediction.**

112 The thermodynamic model ISORROPIA-II was used to estimate the pH value of the
113 particles (Fountoukis, 2007) by inputting RH, T, K^+ , Ca^{2+} , Mg^{2+} , total ammonia
114 ($\text{TNH}_x = 17 \times (\frac{[\text{NH}_4^+]}{18} + \frac{[\text{NH}_3]}{17})$), total sulfuric acid (TH_2SO_4 , SO_4^{2-}), total sodium
115 (TNa , Na^+), total chlorine (TCl , Cl^-), and total nitrate ($\text{TNO}_3 = \text{NO}_3^- + \text{HNO}_3$). The
116 model has two calculation modes: the forward mode and reverse mode, and the aerosol

117 dissolution systems can be set to simulate a metastable state (aqueous phase) or stable
 118 state (aqueous and solid phase). Studies have shown that the forward mode is less
 119 affected by instrument measurement errors than the reverse mode (Ding et al., 2019;
 120 Song et al., 2018). Additionally, the minimum average RH of about 55% was recorded
 121 during the sampling period at the ten sites. Thus, ISORROPIA-II was run in the forward
 122 model for the aerosol system in the metastable condition and only used data with RH \geq
 123 30% for simulation accuracy (Ding et al., 2019; Song et al., 2018). The ISORROPIA
 124 model calculated the particle hydrate ion concentration per volume of air (H_{air^+}) and
 125 aerosol water associated with inorganic matter (AWC_{inorg}). The pH value was calculated
 126 using the following equation (Bougiatioti et al., 2016):

$$127 \quad \text{pH} = -\log_{10} H_{\text{aq}}^+ = -\log_{10} \frac{1000H_{\text{air}}^+}{AWC_{\text{inorg}} + AWC_{\text{org}}} \quad (2.1)$$

128 where the modeled concentrations for AWC_{inorg} and H_{air^+} are $\mu\text{g}/\text{m}^3$, and AWC_{org} is the
 129 particle water associated with the organic matters predicted using the following method:

$$130 \quad AWC_{\text{org}} = \frac{m_s}{\rho_s} \frac{k_{\text{org}}}{\left(\frac{1}{\text{RH}} - 1\right)} \quad (2.2)$$

131 where m_s is the mass concentration of organic matter ($\text{OM} = \text{OC} \times f$). The f is the
 132 conversion factor of OC, which is dependent on the extent of OM oxidation and
 133 secondary organic aerosol formation (Chow et al., 2015). Studies on the ratio of
 134 OM/OC in fourteen cities in China suggested that the mean value of f was 1.59 ± 0.18
 135 during the winter season in Northern China (Xing et al., 2013), and thus we adopted 1.6
 136 as the f in this study. k_{org} is the organic hygroscopicity parameter and depends on organic
 137 functionality, water solubility, molecular weight, and oxidation level. Han et al. (2022)

138 have reported that the k_{org} generally increased with O: C ratios, with a range of 0–0.3
139 for 23 organics, including carboxylic acids, amino acids, sugars, and alcohols. Gunthe
140 et al, (2011) estimated a $k_{org} = 0.06 \pm 0.01$ for the effective average hygroscopicity of
141 the non-refractory organic particulate matter in the aerosols in Beijing. Our previous
142 study has estimated that the uncertainties of k_{org} value (0.06) for pH in the range of 0–
143 0.3 only lead to –1–3% errors, which can be neglected (Wang et al., 2023a). Therefore,
144 the value of 0.06 was selected in this paper. ρ_s is the organic density, which was chosen
145 to be 1.35 g/cm³ following previous studies (Table S2).

146 2.3.2 The sources of HONO

147 The sources of HONO include direct emission (P_{emi}), the homogeneous reaction of
148 NO and •OH (P_{OH+NO}), the heterogeneous reaction of NO₂ on the ground (P_{ground}) and
149 aerosol ($P_{aerosol}$), the photo-enhanced heterogeneous reaction of NO₂ on the ground
150 ($P_{ground+hv}$) and aerosol ($P_{aerosol+hv}$), and nitrate photolysis ($P_{nitrate}$). The detailed
151 calculation method is described in the Supplementary Material (Text S4, Table S3, Figs.
152 S2 and S3)

153 2.3.3 Redox reaction of NO₂ with SO₂.

154 The redox reaction of NO₂ with SO₂ (R₁) is considered a crucial potential source of
155 high concentrations of HONO in Northern China (Cheng et al., 2019; Wang et al.,
156 2016b):



158 the rate expression for reaction (R₁) was estimated to:

159
$$d[S(VI)] / dt = k_1[NO_2][S(VI)], \quad (2.3)$$

160 the rate constant k_1 value is pH dependent, e.g., for pH, 5, $k_1 = (1.4 \times 10^5 + 1.24 \times 10^7)/2$
161 $M^{-1} s^{-1}$. For k_1 values under other pH conditions and other related information, please
162 refer to Text S5, Table S4, and Table S5.

163 **3. Results and discussion**

164 **3.1 Variations of NH₃, NH₄⁺ and TNH_x.**

165 The temporal variations of NH₃, NH₄⁺, and TNH_x at 10 sampling sites in the pre-
166 COVID-19 pandemic period (PC, January 1 to 23, 2020) and during the COVID-19
167 pandemic period (DC, January 24 to February 29, 2020) are presented in Fig. 1, with
168 their average concentration listed in Table 1. In general, rural sites exhibited higher
169 concentrations of NH₃, NH₄⁺, and TNH_x compared to urban sites, except for the R-NY
170 site. This finding is consistent with previous studies conducted in Zhengzhou (Wang et
171 al., 2020), Shanghai (Chang et al., 2019), and Quzhou (Feng et al., 2022a), owing to
172 the intense agricultural ammonia emissions. The highest concentrations of NH₃ and
173 TNH_x were recorded at site R-JZ, with average values of 25.3 ± 11.5 and 40.8 ± 20.1
174 $\mu g/m^3$, respectively. Site R-AY had the highest NH₄⁺ concentration, measuring $19.3 \pm$
175 $12.9 \mu g/m^3$. Note that the current study area exhibited higher NH₃ levels compared to
176 other regions (Table S6), which probably was attributed to the highest NH₃ emissions
177 of Henan Province in China, primarily from nitrogen fertilizer application and livestock
178 farming (Wang et al., 2018; Ma, 2020).

179 Compared to the PC, NH₃ concentrations increased in the DC at all sites. Notably,
180 rural sites experienced more significant increases in NH₃ concentrations than urban
181 sites, which was similar to the trend in Shanghai (Xu et al., 2022). The largest increases
182 in NH₃ concentrations were observed at R-SQ (71%, 7.3 µg/m³) and U-ZK (37%, 4.8
183 µg/m³) for rural and urban sites, respectively. In contrast, the concentrations of NH₄⁺
184 and TNH_x decreased in the DC with the largest reduction at rural site R-PY (51%, 12.9
185 µg/m³) and urban site U-ZMD (48%, 9.3 µg/m³). Regarding TNH_x, rural sites exhibited
186 larger reductions, with site R-SQ experiencing the largest decrease of 37% (4.7 µg/m³).

187 Figure 2 illustrates the spatial distribution and the diurnal variation of NH₃
188 concentrations at the ten sites before and during the pandemic. NH₃ concentrations in
189 most sites exhibited an unimodal trend in PC that NH₃ concentrations gradually
190 increased after sunrise, reaching a peak around noon (11:00–12:00), and then decreased
191 to a valley around 16:00–17:00. This diurnal pattern is similar to NH₃ variations
192 observed in urban areas of Houston, USA, as a result of the natural emissions from
193 vegetation and soil during photosynthesis (Gong et al., 2011). However, other studies
194 have recorded a significant NH₃ peak during the early morning of 8:00–10:00 (Ellis et
195 al., 2011; Meng et al., 2018; Gu et al., 2022), suggesting the influence of vehicle
196 emissions (Gong et al., 2011; Gu et al., 2022), residual NH₃ mixing, soil or plant
197 emissions (Ellis et al., 2011), and dew volatilization (Wentworth et al., 2016; Huang et
198 al., 2021b). Therefore, the NH₃ in urban and rural areas of this study was probably less
199 affected by NH₃ emissions from vehicles, different from the recent studies in megacities
200 of China (e.g., Beijing and Shanghai) (Gu et al., 2022; Wu et al., 2023; Zhang et al.,

201 2020b). In addition to the transport from agricultural emissions, urban NH₃ in this
202 region might also originate from other non-agricultural sources, such as wastewater
203 treatment, coal combustion, household waste, urban green spaces, and human
204 excrement (Chang et al., 2019).

205 During the COVID-19 pandemic, the diurnal variation of NH₃ in both urban and rural
206 sites still maintained a unimodal distribution. The peak values in urban sites remained
207 consistent with PC levels, further demonstrating that the influence of vehicles on NH₃
208 in urban areas was limited. Notably, the peak time of NH₃ in rural sites shifted 1–2 hours
209 earlier compared to the trend in PC. Ammonia in rural areas primarily originates from
210 nitrogen fertilizer application, livestock, and poultry breeding (Feng et al., 2022b;
211 Meng et al., 2018), which are significantly influenced by T and RH (Liu et al., 2023).
212 Table S7 and Fig. S4 reveal that there was an increased T and a decreased RH at rural
213 sites in the DC than the PC, which could accelerate the evaporation of NH₃ and thus
214 potentially lead to earlier peak NH₃ concentrations.

215 **3.2 Gas-to-particle conversion of NH₃**

216 **The increased NH₃ accompanying decreased NH₄⁺ in the DC suggests that the gas-**
217 **particle partition of NH₃/ NH₄⁺ may determine the elevated NH₃ concentrations.**

218 Meteorological parameters, including RH and T, play a crucial role in the gas-particle
219 partitioning of NH₃ (Liu et al., 2023; Xu et al., 2020). Therefore, the higher T and lower
220 RH in the DC (Table S7 and Fig. S4) favored the conversion of NH₄⁺ to NH₃, resulting
221 in a decrease in $\epsilon(\text{NH}_4^+)$ ($[\text{NH}_4^+]/([\text{NH}_3] + [\text{NH}_4^+])$) compared to those in the PC (Table

222 S7).

223 NH₃ primarily enters particles to neutralize acidic ions (Wang et al., 2020; Xu et al.,
224 2020; Liu et al., 2017; Ye et al., 2011; Wells, 1998). Accordingly, the concentrations of
225 required ammonia (Required-NH_x) and excess ammonia (Excess-NH_x) were calculated
226 based on the acidic substances as follows (Wang et al., 2020):

$$\begin{aligned} \text{Required-NH}_x = & 17 \times \left(\frac{[\text{SO}_4^{2-}]}{48} + \frac{[\text{NO}_3^-]}{63} + \frac{[\text{Cl}^-]}{35.5} + \frac{[\text{HNO}_3]}{64} + \frac{[\text{HCl}]}{36.5} \right) \\ & - 17 \times \left(\frac{[\text{Na}^+]}{23} + \frac{[\text{K}^+]}{39} + \frac{[\text{Ca}^{2+}]}{20} + \frac{[\text{Mg}^{2+}]}{12} \right) \end{aligned} \quad (3.1)$$

$$\text{Excess-NH}_x = \text{TNH}_x - \text{Required-NH}_x \quad (3.2)$$

229 where [W] represents the concentration of the substance (μg/m³). The significant linear
230 fitting (R² is greater than 0.96, and the slope is close to 1) in Fig. S5 demonstrates that
231 the anions and cations at each site were close to the equilibrium state. Therefore, the
232 organic acids in PM_{2.5} may have less effect on NH₃ and NH₄⁺ and were not considered
233 in Formula 3.1.

234 As shown in Fig. 3 and Table S8, compared to those in the PC, the concentration of
235 Required-NH_x in the DC significantly decreased (ranging from 37% at site R-JZ to 58%
236 at site R-PY), while the concentration of Excess-NH_x increased (ranging from 9% at
237 site R-AY to 78% at site R-SQ). The reduction in the concentrations of sulfate and
238 nitrate (Fig. S6) was responsible for the decrease in the concentration of Required-NH_x.
239 To sum up, in addition to meteorological conditions, the substantial reduction in
240 anthropogenic emissions of SO₂, NO_x, and other pollutants in the DC had led to a
241 decrease in acidic substances (e.g., sulfate and nitrate) in particles, in turn, resulting in
242 more gas-phase NH₃ concentration remaining in the atmosphere.

243 3.3 Particle pH before and during COVID-19

244 Diurnal patterns of particle pH in PC and DC at ten sites are summarized in Fig. 4
245 with their average values listed in Table S9. $PM_{2.5}$ shows consistent moderate acidity,
246 with mean values in the range of 4.2–5.1, which were close to the values in previous
247 studies (Table S9). Compared to the PC, the particle pH at ten sites increased obviously
248 in the DC, with the highest increase of 0.5 (U-ZK) and 0.3 (R-PY) at urban and rural
249 sites, respectively, which were the subject of in-depth discussion in the following text.

250 To explore the dominant factors that determine the local particle pH level and result
251 in the high pH during the DC, sensitivity tests of pH to chemical species (i.e., TNH_x ,
252 TH_2SO_4 , TNO_3 , TCl, TNa, K^+ , Ca^{2+} , and Mg^{2+}) and meteorological parameters (i.e., T
253 and RH) were performed. A given range for a variable (i.e., TNH_x) with corresponding
254 average values of other parameters (i.e., TH_2SO_4 , TNO_3 , TCl, TNa, K^+ , Ca^{2+} , Mg^{2+} , T,
255 and RH) was input into the model and simulated to compare its effects on pH. As shown
256 in Fig. S7, pH increases with the cation concentrations (i.e., TNH_x , Na^+ , K^+ , Ca^{2+} , and
257 Mg^{2+}) increasing as well as the anion concentrations (i.e., TH_2SO_4 , TNO_3 , and Cl⁻), T
258 and RH decreasing. According to the average values of input data during PC (Blue line
259 in Fig. S7) and DC (Red line in Fig. S7) at U-ZK and R-PY sites respectively, the
260 changes in pH (ΔpH in Fig. 5) indicate that the decrease in TNH_x concentration and the
261 increase in T in DC led to a decrease in pH values (ΔpH : 0.09 at U-ZK and 0.08 at R-
262 PY sites) compared to PC. However, this effect was outweighed by the decrease in
263 TH_2SO_4 (ΔpH : 0.07 and 0.8 at U-ZK and R-PY sites, respectively) and TNO_3 (ΔpH :
264 0.05 and 0.4 at U-ZK and R-PY sites, respectively) concentrations as well as the

265 increase in K^+ (ΔpH : 0.03 at U-ZK and 0.2 at R-PY site) and Mg^{2+} (ΔpH : 0.01 at U-ZK
266 and 0.04 at R-PY site) concentrations in the DC, and resulting in an overall increase in
267 pH values in the DC. Furthermore, the relationship between particle pH with the
268 concentrations of Required- NH_x , and Excess- NH_x , which considers all chemical
269 components, is investigated to examine the dominant factor on the increasing pH in DC.
270 As shown in Fig. 6, the higher Excess- NH_x concentrations in the DC led to higher
271 increases in pH values (ΔpH : 1 at U-ZK and 0.5 at R-PY site) than those in PC (ΔpH :
272 0.3 at U-ZK and 0.2 at R-PY site), thus Excess- NH_x concentrations may be the key
273 factor in promoting the pH values.

274 **3.4 The influence of pH on HONO.**

275 The observed HONO concentrations decreased by 18% and 54% at U-ZK (0.8 ppb)
276 and R-PY (0.9 ppb) sites in the DC, respectively, compared to those (1.0 and 2.2 ppb)
277 in the PC. Moreover, all the known HONO production sources rates including P_{emi} , P_{OH}
278 $+ \text{NO}$, P_{ground} , $P_{\text{ground+hv}}$, P_{aerosol} , $P_{\text{aerosol+hv}}$, and P_{nitrate} (Fig. 7) show a decreasing trend from
279 PC to DC, with the total reductions of 42% and 80% for U-ZK and R-PY, respectively.
280 At the U-ZK, $P_{\text{ground+hv}}$ decreased the most (84%), while at the R-PY, P_{nitrate} had the
281 largest decrease about 85%, which was speculated to be related to the decrease of NO_x
282 and NO_3^- concentration in DC. Note that the reduction rates in the overall known source
283 and almost individual sources were greater than the reduction rates in HONO
284 concentrations (Figs. 7 and 8), thus we hypothesized that there should be other sources
285 capable of promoting HONO production. Soil emission has been demonstrated to be a

286 major source of HONO, which is affected by temperature to some extent (Liu et al.,
287 2020b, 2020c). However, there was no significant positive correlation with temperature
288 in Fig. S8, and temperatures did not exceed 10°C during the study periods, suggesting
289 that soil emission may not be a major contributor to HONO. Note that there were
290 positive correlations between HONO with SO₂, Excess-NH_x, SO₄²⁻, and pH (Fig. S8)
291 indicating that the R₁ reaction might form an amount of HONO and contribute to less
292 reduction in the observed HONO concentrations.

293 Considering that R₁ mainly reacts in the liquid phase, the calculated reaction rates of
294 R₁ under the conditions of RH > 60% in the PC and DC periods are illustrated in Figs.
295 8 and S9. Despite the decrease in NO₂ and SO₂ concentrations in the DC, the increase
296 in particle pH, increasing HSO₃⁻ concentration in the aqueous phase, promoted the R₁
297 reaction rates by 58% and 59% at U-ZK and R-PY (Figure 8), respectively.
298 Consequently, the enhanced R₁ reaction might prevent a large decrease in HONO (18%
299 at U-ZK and 53% at R-PY) under the conditions of a significant reduction in vehicle
300 emissions and a decline of 66% and 69% in NO₂ concentrations at U-ZK and R-PY,
301 respectively.

302 3.5 Uncertainty

303 According to sensitivity tests of pH (Fig. S7) and R₁ (Fig. S10), pH increases with
304 the concentrations of cations (TNH_x, TNa, K⁺, Ca²⁺, and Mg²⁺) and OC increasing as
305 well as anions (TH₂SO₄, TNO₃, and Cl⁻) concentrations, T, and RH decreasing. R₁
306 reaction rate increases with the concentrations of AWC, NO₂, SO₂, pH, and pressure,

307 while increasing as well as T decreasing. Therefore, two extreme scenarios (i.e., the
308 maximum and minimum rate scenarios) were evaluated to estimate the uncertainty of
309 pH, and R_1 based on the measurement uncertainties at the U-ZK and R-PY sites. Figure
310 S11 suggests that the two extreme scenarios can be led to $-10\text{--}7\%$ and $-71\text{--}125\%$
311 uncertainties at the U-ZK site and $-10\text{--}7\%$ and $-78\text{--}123\%$ uncertainties at the R-PY
312 site for pH and R_1 , respectively.

313 **4. Conclusions**

314 Elevated NH_3 concentration was observed during the COVID-19 pandemic at both
315 urban and rural sites in China. In addition to the rise in T and decrease in RH during the
316 COVID-19 pandemic, which favored the conversion of NH_4^+ to NH_3 , the significant
317 decrease in sulfate and nitrate concentrations led to the decline in Required- NH_x and
318 was beneficial to the particle-phase NH_4^+ partitioning to gas-phase NH_3 . Furthermore,
319 under the environmental conditions of increased NH_3 concentration and decreased
320 acidic substance concentration, the pH values increased by 0.5 and 0.3 at U-ZK and R-
321 PY increased during the pandemic, respectively. Consequently, the high pH values
322 accelerated the formation rate of HONO through the oxidation-reduction reaction of
323 NO_2 with SO_2 (an increase of 58% at U-ZK and 59% at R-PY, respectively), partially
324 compensating for the decrease in HONO concentration caused by the decline in vehicle
325 emissions, NO_2 and NO_3^- concentrations during the COVID-19 pandemic.

326 **5. Implications**

327 HONO plays a crucial role as a precursor to OH radicals in the tropospheric
328 atmosphere (Xue, 2022). There have been significant observations of high HONO
329 concentrations in urban areas during the daytime, leading to a growing interest in
330 understanding its sources in atmospheric chemistry (Jiang et al., 2022; Xu et al., 2019).
331 The heterogeneous reaction mechanism of NO₂ on aerosol surfaces is currently the
332 focus of research on HONO sources, particularly in regions with elevated levels of
333 atmospheric particulate matter, where it could potentially become a major contributor
334 to HONO production (Zhang et al., 2022; Liao et al., 2021). One of the pathways for
335 heterogeneous reactions on aerosol surfaces is the redox reaction of NO₂ with SO₂.
336 However, the significance of this reaction in HONO production in the real atmosphere
337 is often overlooked, as it relies on the high pH of aerosols (Ge et al., 2019). In recent
338 years, there has been increasing attention on the enhancing effect of NH₃ on the redox
339 reaction, with laboratory experiments demonstrating its ability to generate substantial
340 amounts of HONO (Ge et al., 2019). This study highlights the importance of this
341 reaction based on actual atmospheric observations. Furthermore, numerous studies
342 have indicated that if control over NH₃ emissions continues to relax while SO₂ and NO₂
343 emissions decrease, the particle pH in future China is expected to rise steadily (Xie et
344 al., 2020; Song et al., 2019; Wang et al., 2020). **Consequently, the redox reaction of**
345 **NO₂ with SO₂ could become a significant source of HONO in China.** Therefore, it is
346 crucial to coordinate the control of SO₂, NO_x, and NH₃ emissions to avoid a rapid
347 increase in the particle pH.

348

349 **Data availability:** All the data presented in this article can be accessed through
350 <https://zenodo.org/records/10273539>. (Zhang, 2023).

351

352 **Author contributions.** XZ Data Curation, Writing - Original Draft, Visualization.
353 LW, NW, SM, and DZ Investigation, Visualization, Data Curation. DZ, HZ, and MW
354 Investigation. SW Conceptualization, Data Curation, Supervision. RZ Data Curation,
355 Funding acquisition. All people are involved in the discussion of the results.

356

357 **Competing interest.** The authors declare no competing financial interest.

358

359 **Acknowledgments.** This work was supported by the China Postdoctoral Science
360 Foundation (2023M733220), the Zhengzhou PM_{2.5} and O₃ Collaborative Control and
361 Monitoring Project (20220347A), and the National Key Research and Development
362 Program of China (No. 2017YFC0212403).

363 **References**

- 364 Alicke, B.: OH formation by HONO photolysis during the BERLIOZ experiment, J.
365 Geophys. Res.; 108, 8247, <https://doi.org/10.1029/2001JD000579>, 2003.
- 366 Atkinson, R., Baulch, D.L., Cox, R.A., Crowley, J.N., Hampson, R.F., Hynes, R.G.,
367 Jenkin, M.E., and Rossi, M. J., Troe, J.: Evaluated kinetic and photochemical data
368 for atmospheric chemistry: volume I - gas phase reactions of O_x, HO_x, NO_x and
369 SO_x species., Atmos. Chem. Phys., 4,1461–1738, [https://doi.org/10.5194/acp-4-](https://doi.org/10.5194/acp-4-1461-2004)
370 [1461-2004](https://doi.org/10.5194/acp-4-1461-2004), 2004.
- 371 Bougiatioti, A., Nikolaou, P., Stavroulas, I., Kouvarakis, G., Weber, R., Nenes, A.,
372 Kanakidou, M., and Mihalopoulos, N.: Particle water and pH in the eastern
373 Mediterranean: source variability and implications for nutrient availability, Atmos.
374 Chem. Phys., 16, 4579–4591, <https://doi.org/10.5194/acp-16-4579-2016>, 2016.
- 375 Chang, Y., Zou, Z., Zhang, Y., Deng, C., Hu, J., Shi, Z., Dore, A. J., and Collett, J. L.,
376 Jr.: Assessing contributions of agricultural and nonagricultural emissions to
377 atmospheric ammonia in a Chinese megacity. Environ. Sci. Technol. 53, 1822–
378 1833., <https://doi.org/10.1021/acs.est.8b05984>, 2019.
- 379 Chen, X., Walker, J. T., and Geron, C.: Chromatography related performance of the
380 monitor for aerosols and gases in ambient air (MARGA): laboratory and field-
381 based evaluation. Atmos. Meas. Tech. 10, 3893–3908.
382 <https://doi.org/10.5194/amt-10-3893-2017>, 2017.
- 383 Cheng, Y., Zheng, G., Wei, C., Mu, Q., Zheng, B., Wang, Z., Gao, M., Z., Q., He, K.,
384 Carmichael, G., Pöschl, U., and Su, and H.: Reactive nitrogen chemistry in aerosol

385 water as a source of sulfate during haze events in China, *Sci. Adv.* 2, e1601530.,
386 <https://doi.org/10.1126/sciadv.1601530>, 2019.

387 Chow, J. C., Lowenthal, D. H., Chen, L. W. A., Wang, X., and Watson, J. G.: Mass
388 reconstruction methods for PM_{2.5}: a review, *Air Qual. Atmos. Health.*, 8, 243 – 263,
389 <https://doi.org/10.1007/s11869-015-0338-3>, 2015.

390 Cui, L.: Impact of COVID-19 restrictions on the concentration and source
391 apportionment of atmospheric ammonia (NH₃) across India, *Sci. Total Environ.*,
392 881, <https://doi.org/10.1016/j.scitotenv.2023.163443>, 2023.

393 Ding, J., Zhao, P., Su, J., Dong, Q., Du, X., and Zhang, Y.: Aerosol pH and its driving
394 factors in Beijing, *Atmos. Chem. Phys.* 19, 7939–7954.,
395 <https://doi.org/10.5194/acp-19-7939-2019>, 2019.

396 Ellis, R. A., Murphy, J. G., Markovic, M. Z., VandenBoer, T. C., Makar, P. A., Brook,
397 J., and Mihele, C.: The influence of gas-particle partitioning and surface-
398 atmosphere exchange on ammonia during BAQS-Met, *Atmos. Chem. Phys.* 11,
399 133–145., <https://doi.org/10.5194/acp-11-133-2011>, 2011.

400 Feng, S., Xu, W., Cheng, M., Ma, Y., Wu, L., Kang, J., Wang, K., Tang, A., Collett, J.
401 L., Fang, Y., Goulding, K., Liu, X., and Zhang, F.: Overlooked nonagricultural and
402 wintertime agricultural NH₃ emissions in Quzhou county, north China plain:
403 evidence from ¹⁵N-Stable Isotopes. *Environ. Sci. Technol. Lett.* 9, 127–133,
404 <https://doi.org/10.1021/acs.estlett.1c00935>, 2022a.

405 Feng, T., Zhao, S., Liu, L., Long, X., Gao, C., and Wu, N.: Nitrous acid emission from
406 soil bacteria and related environmental effect over the North China Plain, *Chemos.*,
407 287, <https://doi.org/10.1016/j.chemosphere.2021.132034>, 2022b.

408 Fountoukis, C., Nenes, A.: ISORROPIA II: a computationally efficient thermodynamic

409 equilibrium model for K^+ - Ca^{2+} - Mg^{2+} - NH_4^+ - Na^+ - SO_4^{2-} - NO_3^- - Cl^- - H_2O aerosols.
410 Atmos. Chem. Phys. 7, 4639–4659, <https://doi.org/10.5194/acp-7-4639-2007>,
411 2007.

412 Ge, S., Wang, G., Zhang, S., Li, D., and Zhang, H.: Abundant NH_3 in China enhances
413 atmospheric HONO production by promoting the heterogeneous reaction of SO_2
414 with NO_2 . Environ. Sci. Technol. 53, 14339–14347,
415 <https://doi.org/10.1021/acs.est.9b04196>, 2019.

416 Gong, L., Lewicki, R., Griffin, R. J., Flynn, J. H., Lefer, B. L., and Tittel, F. K.:
417 Atmospheric ammonia measurements in Houston, TX using an external-cavity
418 quantum cascade laser-based sensor, Atmos. Chem. Phys. 11, 9721–9733,
419 <https://doi.org/10.5194/acp-11-9721-2011>, 2011.

420 Gu, M., Pan, Y., Walters, W. W., Sun, Q., Song, L., Wang, Y., Xue, Y., and Fang, Y.:
421 vehicular emissions enhanced ammonia concentrations in winter mornings: insights
422 from diurnal nitrogen isotopic signatures. Environ. Sci. Technol. 56, 1578–1585,
423 <https://doi.org/10.1021/acs.est.1c05884>, 2022.

424 Gunthe, S. S., Rose, D., Su, H., Garland, R. M., Achtert, P., Nowak, A., Wiedensohler,
425 A., Kuwata, M., Takegawa, N., Kondo, Y., Hu, M., Shao, M., Zhu, T., Andreae, M.
426 O., and Pöschl, U.: Cloud condensation nuclei (CCN) from fresh and aged air
427 pollution in the megacity region of Beijing, Atmos. Chem. Phys., 11, 11023 –
428 11039, <https://doi.org/10.5194/acp-11-11023-2011>, 2011.

429 Han, S., Hong, J., Luo, Q., Xu, H., Tan, H., Wang, Q., Tao, J., Zhou, Y., Peng, L., He,
430 Y., Shi, J., Ma, N., Cheng, Y., and Su, H.: Hygroscopicity of organic compounds
431 as a function of organic functionality, water solubility, molecular weight, and

432 oxidation level, *Atmos. Chem. Phys.*, 22, 3985–4004, <https://doi.org/10.5194/acp->
433 [22-3985-2022](https://doi.org/10.5194/acp-22-3985-2022), 2022.

434 Huang, X., Ding, A., Gao, J., Zheng, B., Zhou, D., Qi, X., Tang, R., Wang, J., Ren, C.,
435 Nie, W., Chi, X., Xu, Z., Chen, L., Li, Y., Che, F., Pang, N., Wang, H., Tong, D.,
436 Qin, W., Cheng, W., Liu, W., Fu, Q., Liu, B., Chai, F., Davis, S. J., Zhang, Q., and
437 He, K.: Enhanced secondary pollution offset reduction of primary emissions
438 during COVID-19 lockdown in China, *Natl Sci Rev*, 8, nwaal37,
439 <https://doi.org/10.1093/nsr/nwaa137>, 2021a.

440 Huang, X., Zhang, J., Zhang, W., Tang, G., and Wang, Y.: Atmospheric ammonia and
441 its effect on PM_{2.5} pollution in urban Chengdu, Sichuan Basin, China. *Environ.*
442 *Pollut.* 291, 118–195. <https://doi.org/10.1016/j.envpol.2021.118195>, 2021b.

443 Jiang, Y., Xue, L., Shen, H., Dong, C., Xiao, Z., and Wang, W.: Dominant processes of
444 HONO derived from multiple field observations in contrasting environments.
445 *Environ. Sci. Technol. Lett.* 9, 258–264,
446 <https://doi.org/10.1021/acs.estlett.2c00004>, 2022.

447 Kleffmann, J., Gavriiloaiei, T., Hofzumahaus, A., Holland, F., Koppmann, R., Rupp, L.,
448 Schlosser, E., Siese, M., and Wahner, A.: Daytime formation of nitrous acid: A
449 major source of OH radicals in a forest, *Geophys. Res. Lett.*, 32,
450 <https://doi.org/10.1029/2005gl022524>, 2005.

451 Kramer, L. J., Crilley, L. R., Adams, T. J., Ball, S. M., Pope, F. D., and Bloss, W. J.:
452 Nitrous acid (HONO) emissions under real-world driving conditions from vehicles
453 in a UK road tunnel, *Atmos. Chem. Phys.* 20, 5231–5248,

454 <https://doi.org/10.5194/acp-20-5231-2020>, 2020.

455 Li, J., An, X., Cui, M., Sun, Z., Wang, C., and Li, Y.: Simulation study on regional
456 atmospheric oxidation capacity and precursor sensitivity, *Atmos. Environ.* 263,
457 118657, <https://doi.org/10.1016/j.atmosenv.2021.118657>, 2021a.

458 Li, S., Song, W., Zhan, H., Zhang, Y., Zhang, X., Li, W., Tong, S., Pei, C., Wang, Y.,
459 Chen, Y., Huang, Z., Zhang, R., Zhu, M., Fang, H., Wu, Z., Wang, J., Luo, S., Fu,
460 X., Xiao, S., Huang, X., Zeng, J., Zhang, H., Chen, D., Gligorovski, S., Ge, M.,
461 George, C., and Wang, X.: Contribution of vehicle emission and NO₂ surface
462 conversion to nitrous acid (HONO) in urban environments: implications from tests
463 in a tunnel. *Environ. Sci. Technol.*, 55, 15616–15624,
464 <https://doi.org/10.1021/acs.est.1c00405>, 2021.

465 Liao, S., Zhang, J., Yu, F., Zhu, M., Liu, J., Ou, J., Dong, H., Sha, Q., Zhong, Z., Xie,
466 Y., Luo, H., Zhang, L., and Zheng, J.: High gaseous nitrous acid (HONO)
467 emissions from light-duty diesel vehicles. *Environ. Sci. Technol.* 55, 200–208,
468 <https://doi.org/10.1021/acs.est.0c05599>, 2021.

469 Liu, J., Deng, H., Lakey, P. S. J., Jiang, H., Mekic, M., Wang, X., Shiraiwa, M., and
470 Gligorovski, S.: Unexpectedly high indoor HONO concentrations associated with
471 photochemical NO₂ transformation on glass windows. *Environ. Sci. Technol.* 54,
472 15680–15688, <https://doi.org/10.1021/acs.est.0c05624>, 2020a.

473 Liu, M., Song, Y., Zhou, T., Xu, Z., Yan, C., Zheng, M., Wu, Z., Hu, M., Wu, Y., and
474 Zhu, T.: Fine particle pH during severe haze episodes in northern China. *Geophys.*
475 *Res. Lett.* 44, 5213–5221, <https://doi.org/10.1002/2017gl073210>, 2017.

476 Liu, P., Chen, H., Song, Y., Xue, C., Ye, C., Zhao, X., Zhang, C., Liu, J., and Mu, Y.:
477 Atmospheric ammonia in the rural North China Plain during wintertime: variations,
478 sources, and implications for HONO heterogeneous formation. *Sci. Total. Environ.*
479 861, 160768, <https://doi.org/10.1016/j.scitotenv.2022.160768>, 2023.

480 Liu, Y., Ni, S., Jiang, T., Xing, S., Zhang, Y., Bao, X., Feng, Z., Fan, X., Zhang, L., and
481 Feng, H.: Influence of Chinese New Year overlapping COVID-19 lockdown on
482 HONO sources in Shijiazhuang, *Sci. Total Environ.*, 745, 141025,
483 <https://doi.org/10.1016/j.scitotenv.2020.141025>, 2020b.

484 Liu, Y., Zhang, Y., Lian, C., Yan, C., Feng, Z., Zheng, F., Fan, X., Chen, Y., Wang, W.,
485 Chu, B., Wang, Y., Cai, J., Du, W., Daellenbach, K. R., Kangasluoma, J., Bianchi,
486 F., Kujansuu, J., Petäjä, T., Wang, X., Hu, B., Wang, Y., Ge, M., He, H., and
487 Kulmala, M.: The promotion effect of nitrous acid on aerosol formation in
488 wintertime in Beijing: The possible contribution of traffic-related emissions,
489 *Atmos. Chem. Phys.*, 20, 13023–13040, [https://doi.org/10.5194/acp-20-13023-](https://doi.org/10.5194/acp-20-13023-2020)
490 [2020](https://doi.org/10.5194/acp-20-13023-2020), 2020c.

491 Liu, Z., Wang, Y., Costabile, F., Amoroso, A., Zhao, C., Huey, L. G., Stickel, R., Liao,
492 J., and Zhu, T.: Evidence of aerosols as a media for rapid daytime HONO
493 production over China, *Environ. Sci. Technol.*, 48, 13023–13040,
494 <https://doi.org/10.1021/es504163z>, 2014.

495 Lu, K., Guo, S., Tan, Z., Wang, H., Shang, D., Liu, Y., Li, X., Wu, Z., Hu, M., and
496 Zhang, Y.: Exploring atmospheric free-radical chemistry in China: the self-
497 cleansing capacity and the formation of secondary air pollution, *Natl. Sci. Rev.*, 6,

498 [579-594, https://doi.org/10.1093/nsr/nwy073](https://doi.org/10.1093/nsr/nwy073), 2018.

499 Luo, L., Bai, X., Lv, Y., Liu, S., Guo, Z., Liu, W., Hao, Y., Sun, Y., Hao, J., Zhang, K.,
500 Zhao, H., Lin, S., Zhao, S., Xiao, Y., Yang, J., and Tian, H.: Exploring the driving
501 factors of haze events in Beijing during Chinese New Year holidays in 2020 and
502 2021 under the influence of COVID-19 pandemic, *Sci. Total Environ.*, 859,
503 160172, <https://doi.org/10.1016/j.scitotenv.2022.160172>, 2023.

504 Ma, S.: High-resolution assessment of ammonia emissions in China: Inventories,
505 driving forces and mitigation, *Atmos. Environ.*, 229,
506 <https://doi.org/10.1016/j.atmosenv.2020.117458>, 2020.

507 McFall, A. S., Edwards, K. C., and Anastasio, C.: Nitrate photochemistry at the air-ice
508 interface and in other ice reservoirs, *Environ. Sci. Technol.*, 52, 5710–5717,
509 <https://doi.org/10.1021/acs.est.8b00095>, 2018.

510 Meng, Z., Xu, X., Lin, W., Ge, B., Xie, Y., Song, B., Jia, S., Zhang, R., Peng, W., Wang,
511 Y., Cheng, H., Yang, W., and Zhao, H.: Role of ambient ammonia in particulate
512 ammonium formation at a rural site in the North China Plain, *Atmos. Chem. Phys.*,
513 18, 167–184, <https://doi.org/10.5194/acp-18-167-2018>, 2018.

514 Meusel, H., Tamm, A., Kuhn, U., Wu, D., Leifke, A. L., Fiedler, S., Ruckteschler, N.,
515 Yordanova, P., Lang-Yona, N., Pöhlker, M., Lelieveld, J., Hoffmann, T., Pöschl,
516 U., Su, H., Weber, B., and Cheng, Y.: Emission of nitrous acid from soil and
517 biological soil crusts represents an important source of HONO in the remote
518 atmosphere in Cyprus, *Atmos. Chem. Phys.*, 18, 799 – 813,
519 <https://doi.org/10.5194/acp-18-799-2018>, 2018.

520 Oswald, R., Behrendt, T., Ermel, M., Wu, D., Su, H., Cheng, Y., Breuninger, C.,
521 Moravek, A., Mougín, E., Delon, C., Loubet, B., Pommerening-Roser, A., Sorgel,

522 M., Poschl, U., and Hoffmann, T., Andreae, M.O., Meixner, F.X., Trebs, I.: HONO
523 emissions from soil bacteria as a major source of atmospheric reactive nitrogen.,
524 Science. 341, 1233–1235, <https://www.science.org/doi/10.1126/science.1242266>,
525 2013.

526 Pagsberg, P., Bjergbakke, E., Ratajczak, E., Sillesen, A.: Kinetics of the gas phase
527 reaction $\text{OH} + \text{NO} (+\text{M}) \rightarrow \text{HONO} (+\text{M})$ and the determination of the UV
528 absorption cross sections of HONO., Chem. Phys. Lett. 272, 383–390,
529 [https://doi.org/10.1016/s0009-2614\(97\)00576-9](https://doi.org/10.1016/s0009-2614(97)00576-9), 1997.

530 Platt, U., Perner, D., Harris, G. W., Winer, A. M., and Pitts, J. N.: Observations of
531 nitrous acid in an urban atmosphere by differential optical absorption, Nature, 285,
532 312–314, <https://doi.org/10.1038/285312a0>, 1980.

533 Romer, P. S., Wooldridge, P. J., Crouse, J. D., Kim, M. J., Wennberg, P. O., Dibb, J.
534 E., Scheuer, E., Blake, D. R., Meinardi, S., Brosius, A. L., Thames, A. B., Miller,
535 D. O., Brune, W. H., Hall, S. R., Ryerson, T. B., and Cohen, R. C.: Constraints on
536 aerosol nitrate photolysis as a potential source of HONO and NO_x . Environ. Sci.
537 Technol. 52, 13738–13746, <https://doi.org/10.1021/acs.est.8b03861>, 2018.

538 Scharko, N. K., Berke, A. E., and Raff, J. D.: Release of nitrous acid and nitrogen
539 dioxide from nitrate photolysis in acidic aqueous solutions, Environ. Sci. Technol.,
540 48, 11991–12001, <https://doi.org/10.1021/es503088x>, 2014.

541 Shi, Q., Tao, Y., Krechmer, J. E., Heald, C. L., Murphy, J. G., Kroll, J. H., and Ye, Q.:
542 Laboratory investigation of renoxification from the photolysis of inorganic
543 particulate nitrate, Environ. Sci. Technol., 55, 854–861,

544 <https://doi.org/10.1021/acs.est.0c06049>, 2021.

545 Song, S., Gao, M., Xu, W., Shao, J., Shi, G., Wang, S., Wang, Y., Sun, Y., and McElroy,
546 M. B.: Fine-particle pH for Beijing winter haze as inferred from different
547 thermodynamic equilibrium models, *Atmos. Chem. Phys.*, 18, 7423–7438,
548 <https://doi.org/10.5194/acp-18-7423-2018>, 2018.

549 Song, S., Nenes, A., Gao, M., Zhang, Y., Liu, P., Shao, J., Ye, D., Xu, W., Lei, L., Sun,
550 Y., Liu, B., Wang, S., and McElroy, M. B.: Thermodynamic modeling suggests
551 declines in water uptake and acidity of inorganic aerosols in Beijing winter haze
552 events during 2014/2015–2018/2019. *Environ. Sci. Technol. Lett.* 6, 752–760,
553 <https://doi.org/10.1021/acs.estlett.9b00621>, 2019.

554 Spataro, F., and Ianniello, A.: Sources of atmospheric nitrous acid: state of the science,
555 current research needs, and future prospects, *J. Air. Waste. Manag. Assoc.*, 64,
556 1232–1250, <https://doi.org/10.1080/10962247.2014.952846>, 2014.

557 Stieger, B., Spindler, G., van Pinxteren, D., Grüner, A., Wallasch, M., and Herrmann,
558 H.: Development of an online-coupled MARGA upgrade for the 2 h interval
559 quantification of low-molecular-weight organic acids in the gas and particle phases,
560 *Atmos. Meas. Tech.* 12, 281–298, <https://doi.org/10.5194/amt-12-281-2019>, 2019.

561 Su, H., Cheng, Y., Oswald, R., Behrendt, T., Trebs, I., Meixner, F.X., Andreae, M.O.,
562 Cheng, P., and Zhang, Y., Poschl, U.: Soil nitrite as a source of atmospheric HONO
563 and OH radicals., *Science*. 333, 1616–1618,
564 <https://doi.org/10.1126/science.1207687>, 2011.

565 Twigg, M. M., Berkhout, A. J. C., Cowan, N., Crunaire, S., Dammers, E., Ebert, V.,

566 Gaudion, V., Haaima, M., Häni, C., John, L., Jones, M. R., Kamps, B., Kentisbeer,
567 J., Kupper, T., Leeson, S. R., Leuenberger, D., Lüttschwager, N. O. B., Makkonen,
568 U., Martin, N. A., Missler, D., Mounsor, D., Neftel, A., Nelson, C., Nemitz, E.,
569 Oudwater, R., Pascale, C., Petit, J.-E., Pogany, A., Redon, N., Sintermann, J.,
570 Stephens, A., Sutton, M. A., Tang, Y. S., Zijlmans, R., Braban, C. F., and
571 Niederhauser, B.: Intercomparison of in situ measurements of ambient NH₃:
572 instrument performance and application under field conditions, *Atmos. Meas.*
573 *Tech.* 15, 6755–6787, <https://doi.org/10.5194/amt-15-6755-2022>, 2022.

574 Wang, C., Yin, S., Bai, L., Zhang, X., Gu, X., Zhang, H., Lu, Q., and Zhang, R.: High-
575 resolution ammonia emission inventories with comprehensive analysis and
576 evaluation in Henan, China, 2006–2016, *Atmos. Environ.* 193, 11–23,
577 <https://doi.org/10.1016/j.atmosenv.2018.08.063>, 2018.

578 Wang, S., Wang, L., Li, Y., Wang, C., Wang, W., Yin, S., and Zhang, R.: Effect of
579 ammonia on fine-particle pH in agricultural regions of China: comparison between
580 urban and rural sites, *Atmos. Chem. Phys.*, 20, 2719–2734,
581 <https://doi.org/10.5194/acp-20-2719-2020>, 2020.

582 Wang, S., Wang, L., Fan, X., Wang, N., Ma, S., and Zhang, R.: Formation pathway of
583 secondary inorganic aerosol and its influencing factors in Northern China:
584 Comparison between urban and rural sites, *Sci. Total Environ.*, 840,
585 <https://doi.org/10.1016/j.scitotenv.2022.156404>, 2022.

586 Wang, S., Fan, X., Xu, Y., Zhang, R., and Ren, B.: Insight into the non-linear responses
587 of particulate sulfate to reduced SO₂ concentration: A perspective from the

588 aqueous-phase reactions in a megacity in Northern China, *Atmos. Res.*, 290,
589 <https://doi.org/10.1016/j.atmosres.2023.106796>, 2023a.

590 Wang, W., Wang, S., Xu, J., Zhou, R., Shi, C., and Zhou, B.: Gas-phase ammonia and
591 PM_{2.5} ammonium in a busy traffic area of Nanjing, China, *Environ. Sci. Pollut.*
592 *Res. Int.*, 23, 1691–1702, <https://doi.org/10.1007/s11356-015-5397-3>, 2016.

593 Wang, Y., Jin, X., Liu, Z., Wang, G., Tang, G., Lu, K., Hu, B., Wang, S., Li, G., An, X.,
594 Wang, C., Hu, Q., He, L., Zhang, F., and Zhang, Y.: Progress in quantitative
595 research on the relationship between atmospheric oxidation and air quality, *J.*
596 *Environ. Sci.*, 123, 350–366, <https://doi.org/10.1016/j.jes.2022.06.029>, 2023b.

597 Wells, M., Choulaton, T. W., and Bower, K. N.: A modelling study of the interaction
598 of ammonia with cloud., *Atmos. Environ.*, 32, 359–363,
599 [https://doi.org/10.1016/s1352-2310\(97\)00199-4](https://doi.org/10.1016/s1352-2310(97)00199-4), 1998.

600 Wentworth, G. R., Murphy, J. G., Benedict, K. B., Bangs, E. J., and Collett Jr, J. L.: The
601 role of dew as a night-time reservoir and morning source for atmospheric ammonia,
602 *Atmos. Chem. Phys.* 16, 7435–7449, <https://doi.org/10.5194/acp-16-7435-2016>,
603 2016.

604 Wu, C., Lv, S., Wang, F., Liu, X., Li, J., Liu, L., Zhang, S., Du, W., Liu, S., Zhang, F.,
605 Li, J., Meng, J., and Wang, G.: Ammonia in urban atmosphere can be substantially
606 reduced by vehicle emission control: A case study in Shanghai, China, *J. Environ.*
607 *Sci.*, 126, 754–760, <https://doi.org/10.1016/j.jes.2022.04.043>, 2023.

608 Xie, Y., Wang, G., Wang, X., Chen, J., Chen, Y., Tang, G., Wang, L., Ge, S., Xue, G.,
609 Wang, Y., and Gao, J.: Nitrate-dominated PM_{2.5} and elevation of particle pH

610 observed in urban Beijing during the winter of 2017. *Atmos. Chem. Phys.* 20,
611 5019–5033, <https://doi.org/10.5194/acp-20-5019-2020>, 2020.

612 Xing, L., Fu, T. M., Cao, J. J., Lee, S. C., Wang, G. H., Ho, K. F., Cheng, M. C., You,
613 C. F., and Wang, T. J.: Seasonal and spatial variability of the OM/OC mass ratios
614 and high regional correlation between oxalic acid and zinc in Chinese urban
615 organic aerosols, *Atmos. Chem. Phys.*, 13, 4307–4318,
616 <https://doi.org/10.5194/acp-13-4307-2013>, 2013.

617 Xu, J., Chen, J., Zhao, N., Wang, G., Yu, G., Li, H., Huo, J., Lin, Y., Fu, Q., Guo, H.,
618 Deng, C., Lee, S.-H., Chen, J., and Huang, K.: Importance of gas-particle
619 partitioning of ammonia in haze formation in the rural agricultural environment,
620 *Atmos. Chem. Phys.* 20, 7259–7269, <https://doi.org/10.5194/acp-20-7259-2020>,
621 2020.

622 Xu, W., Kuang, Y., Zhao, C., Tao, J., Zhao, G., Bian, Y., Yang, W., Yu, Y., Shen, C.,
623 Liang, L., Zhang, G., Lin, W., and Xu, X.: NH₃-promoted hydrolysis of NO₂
624 induces explosive growth in HONO, *Atmos. Chem. Phys.* 19, 10557–10570,
625 <https://doi.org/10.5194/acp-19-10557-2019>, 2019.

626 Xu, W., Zhao, Y., Wen, Z., Chang, Y., Pan, Y., Sun, Y., Ma, X., Sha, Z., Li, Z., Kang, J.,
627 Liu, L., Tang, A., Wang, K., Zhang, Y., Guo, Y., Zhang, L., Sheng, L., Zhang, X.,
628 Gu, B., Song, Y., Van Damme, M., Clarisse, L., Coheur, P. F., Collett, J. L., Jr.,
629 Goulding, K., Zhang, F., He, K., and Liu, X.: Increasing importance of ammonia
630 emission abatement in PM_{2.5} pollution control. *Sci. Bull.* 67, 1745–1749,
631 <https://doi.org/10.1016/j.scib.2022.07.021>, 2022.

632 Xue, C.: Substantially growing interest in the chemistry of nitrous acid (HONO) in
633 China: current achievements, problems, and future directions. *Environ. Sci.*
634 *Technol.* 56, 7375–7377. <https://doi.org/10.1021/acs.est.2c02237>, 2022.

635 Ye, C., Zhang, N., Gao, H., and Zhou, X.: Photolysis of particulate nitrate as a source
636 of HONO and NO_x. *Environ. Sci. Technol.* 51, 6849–6856,
637 <https://doi.org/10.1021/acs.est.7b00387>, 2017.

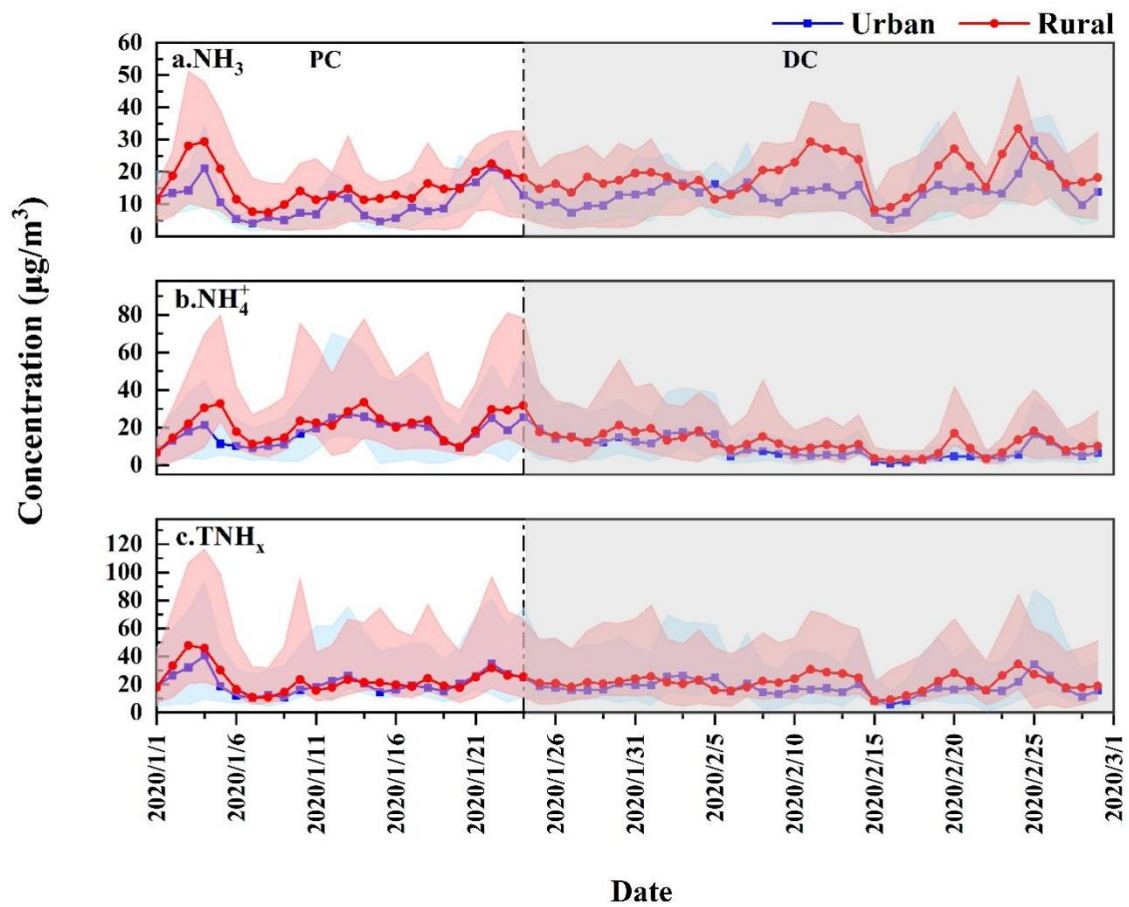
638 Ye, X., Ma, Z., Zhang, J., Du, H., Chen, J., Chen, H., Yang, X., Gao, W., and Geng, F.:
639 Important role of ammonia on haze formation in Shanghai, *Environ. Res. Lett.* 6,
640 024019, <https://doi.org/10.1088/1748-9326/6/2/024019>, 2011.

641 Zhang, W., Tong, S., Jia, C., Wang, L., Liu, B., Tang, G., Ji, D., Hu, B., Liu, Z., Li, W.,
642 Wang, Z., Liu, Y., Wang, Y., and Ge, M.: Different HONO sources for three layers
643 at the urban area of Beijing. *Environ. Sci. Technol.* 54, 12870–12880,
644 <https://doi.org/10.1021/acs.est.0c02146>, 2020a.

645 Zhang, W., Tong, S., Jia, C., Ge, M., Ji, D., Zhang, C., Liu, P., Zhao, X., Mu, Y., Hu, B.,
646 Wang, L., Tang, G., Li, X., Li, W., and Wang, Z.: Effect of different combustion
647 processes on atmospheric nitrous acid formation mechanisms: a winter
648 comparative observation in urban, suburban and rural areas of the North China
649 Plain. *Environ. Sci. Technol.* 56, 4828–4837,
650 <https://doi.org/10.1021/acs.est.1c07784>, 2022.

651 Zhang, Y., Liu, X., Fang, Y., Liu, D., Tang, A., and Collett, J. L.: Atmospheric ammonia
652 in Beijing during the COVID-19 outbreak: concentrations, sources, and
653 implications. *Environ. Sci. Technol. Lett.* 8, 32–38,

655 **Figures:**

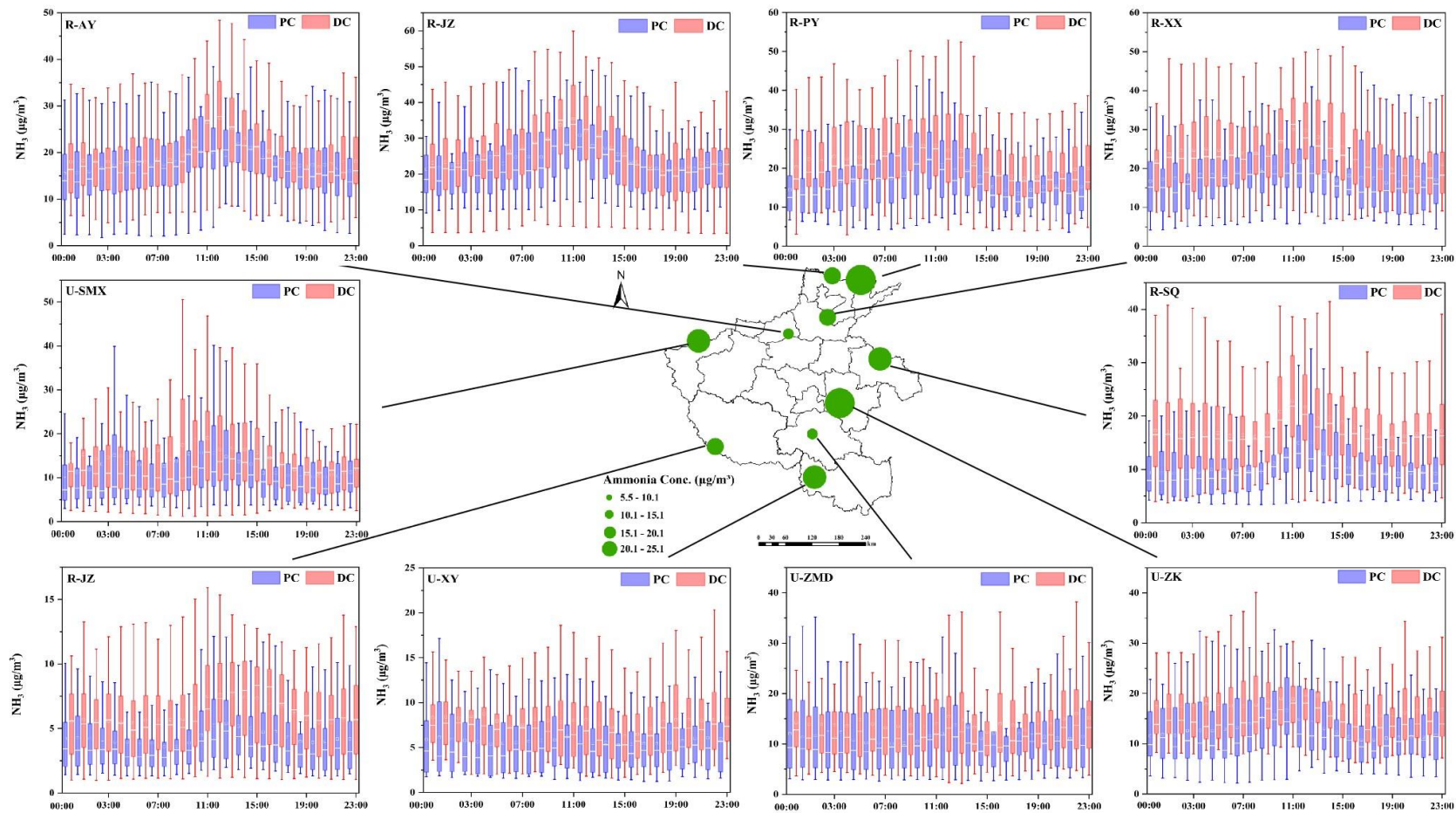


656

657 Figure 1. Temporal variations of a. NH₃, b. NH₄⁺, and c. TNH_x at the urban and rural

658 sites before (PC) and during (DC) the COVID-19 outbreak, respectively. The shaded

659 areas of the curve represent the maximum and minimum values.



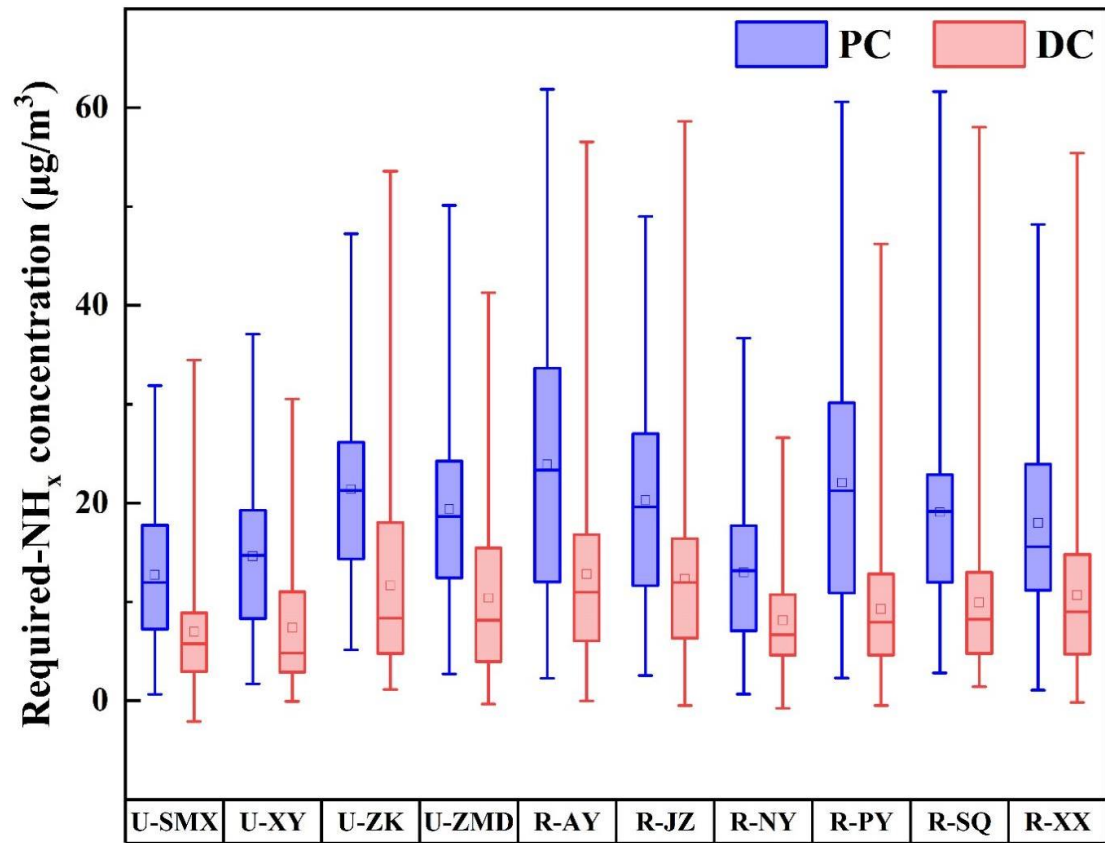
660

661

662

663

Figure 2. Daily variation of NH_3 concentrations at ten sites before (PC) and during (DC) the COVID-19 outbreak. The green dots represent the location of ten sites and their size represents the concentration of NH_3 ; In each box, the top, middle, and bottom lines represent the 75, 50, and 25 percentiles of statistical data, respectively; the upper and lower whiskers represent the 90 and 10 percentiles of statistical data, respectively.



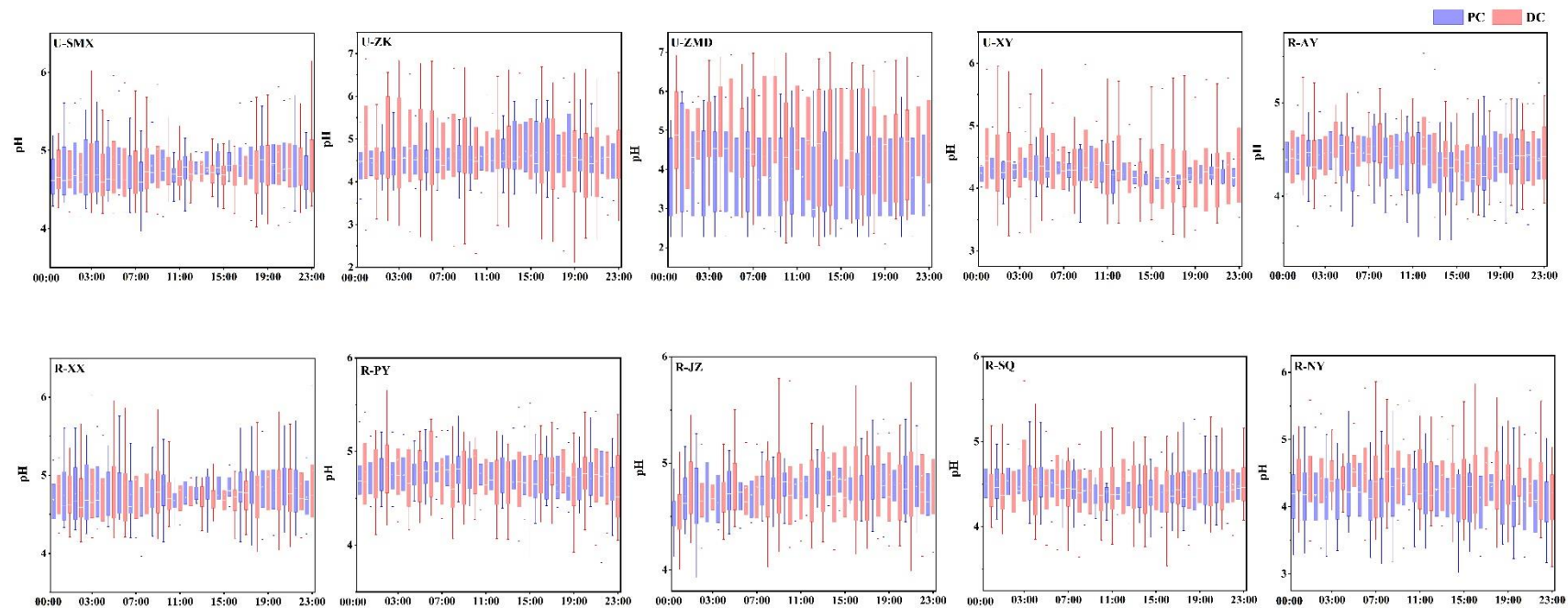
664

665 Figure 3. Box diagram of changes in Required-NH_x at ten sites before (PC) and during

666 (DC) the COVID-19 outbreak. In each box, the top, middle, and bottom lines represent

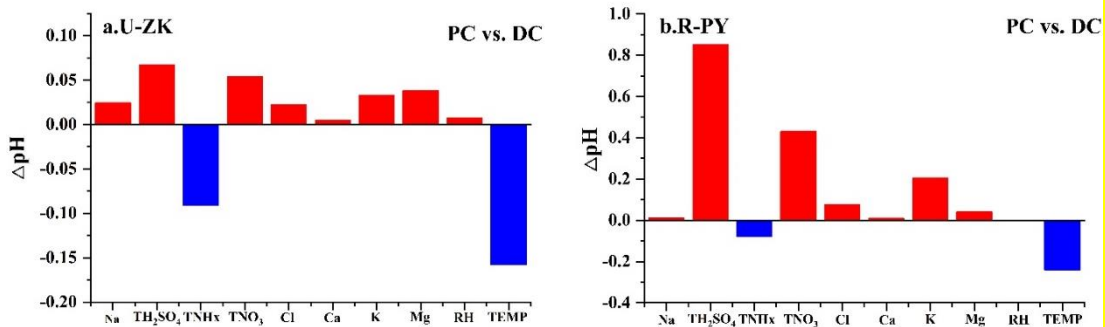
667 the 75, 50, and 25 percentiles of statistical data, respectively; the upper and lower

668 whiskers represent the 90 and 10 percentiles of statistical data, respectively.



669

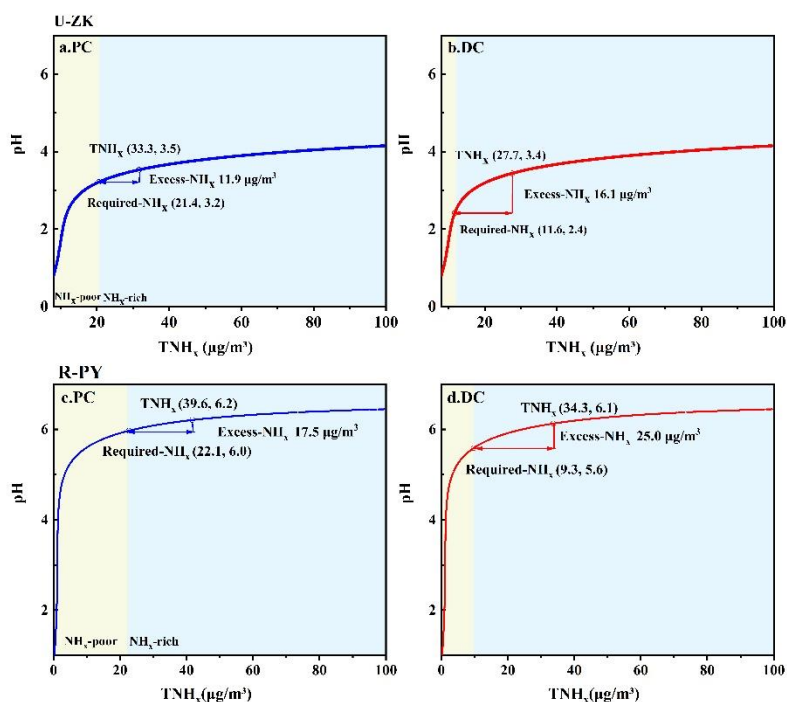
670 Figure 4. Diurnal patterns of pH at ten sites before (PC) and during (DC) the COVID-19 outbreak. In each box, the top, middle, and bottom
 671 lines represent the 75, 50, and 25 percentiles of statistical data, respectively; the upper and lower whiskers represent the 90 and 10 percentiles of
 672 statistical data, respectively.



673

674 Figure 5. Changes of pH (ΔpH) through the sensitivity tests (Figure S5 and S6) by

675 changing parameters between PC and DC at the a. U-ZK and b. R-PY sites.



676

677 Figure 6. Particle pH corresponds to increasing TNH_x at U-ZK and R-PY sites to

678 examine the effects of major indicators of NH_3 (i.e., TNH_x , Required- NH_x , and Excess-

679 NH_x) on aerosol acidity. Particle pH was calculated by using a wide range of TNH_x

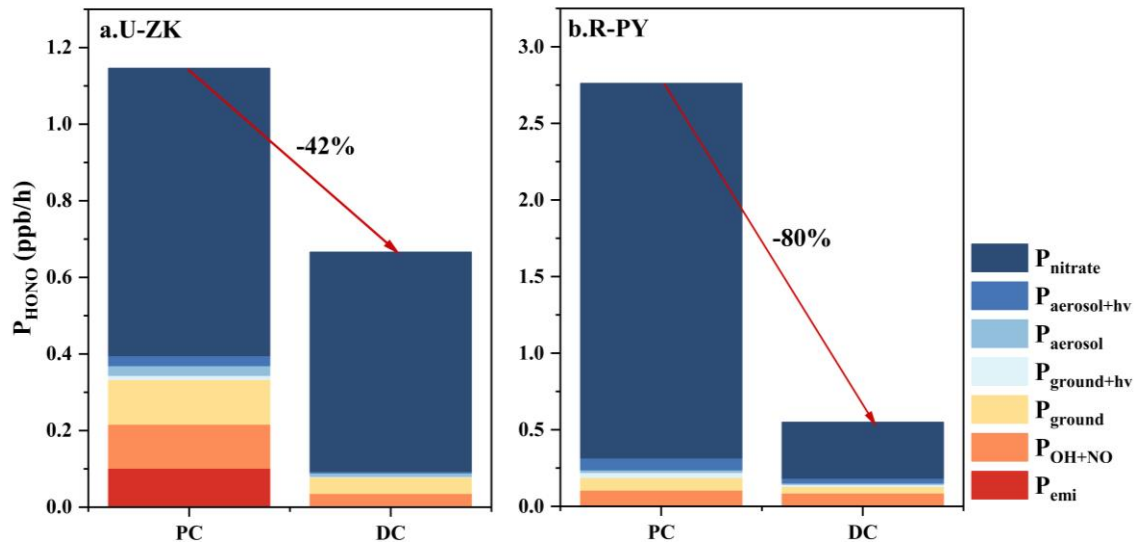
680 ($25\text{--}130\ \mu\text{g}/\text{m}^3$) and average values of other parameters in PC and DC of U-ZK and R-

681 PY sites. The concentrations of TNH_x , Required- NH_x , and Excess- NH_x with

682 corresponding pH values are marked by a hollow box, hollow circle, and arrow

683 respectively. The yellow and blue background colors correspond to the NH_x -poor and

684 NH_x -rich, respectively.

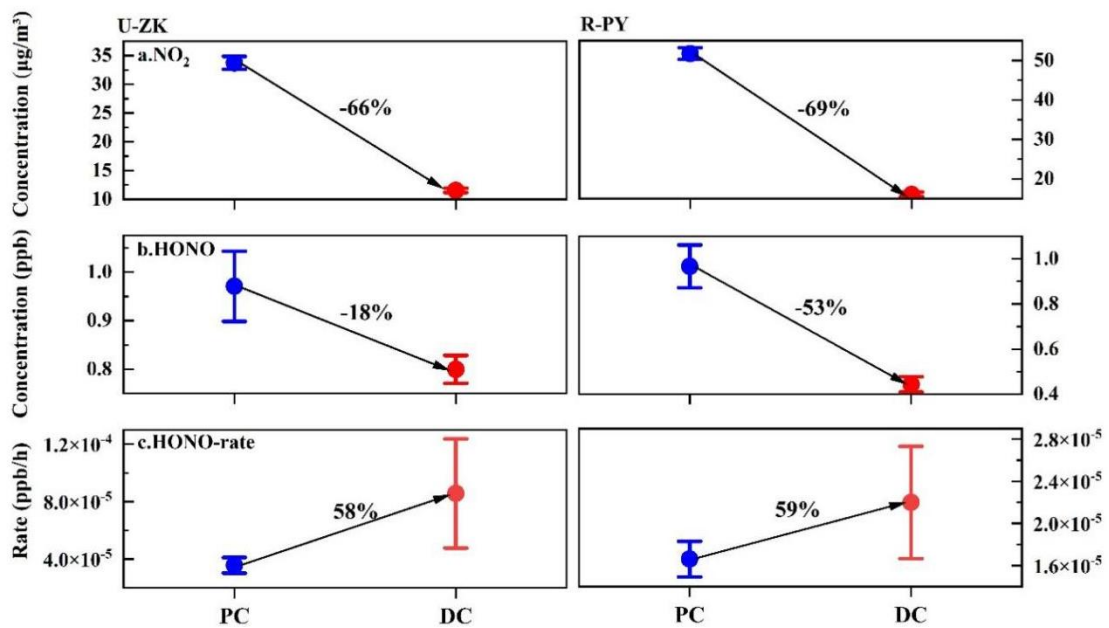


685

686 Figure 7. Comparison of HONO sources at a. U-ZK and b. R-PY sites before (PC) and

687 during (DC) the COVID-19 outbreak. The calculation method can be found in Text S4.

688



689

690 Figure 8. Decline ratios of a. NO_2 , b. HONO concentration, and c. HONO production

691 rate at U-ZK and R-PY sites before (PC) and during (DC) the COVID-19 outbreak. The

692 center point represents the mean value, and the upper and lower whiskers represent the

693 95% confidence interval of the mean.

694 **Table:**

695 Table 1. Changes in concentrations (mean \pm standard deviation) of NH_3 , NH_4^+ , and
 696 TNH_x at ten sites during entire periods (Average), before (PC), and during (DC) the
 697 COVID-19 outbreak.

Sites	Substances	Average ($\mu\text{g}/\text{m}^3$)	PC ($\mu\text{g}/\text{m}^3$)	DC ($\mu\text{g}/\text{m}^3$)
U-SMX	NH_3	13.8 ± 10.8	12.6 ± 10.1	14.5 ± 11.1
	NH_4^+	10.9 ± 7.2	14.2 ± 7.2	8.8 ± 6.5
	TNH_x	22.9 ± 14.1	24.9 ± 14.5	21.7 ± 13.8
U-ZK	NH_3	15.6 ± 8.3	12.7 ± 6.5	17.4 ± 8.8
	NH_4^+	13.6 ± 9.3	19.1 ± 8.4	10.3 ± 8.1
	TNH_x	28.6 ± 13.7	30.9 ± 12.8	27.1 ± 14.0
U-ZMD	NH_3	13.1 ± 8.4	11.6 ± 8.2	14.0 ± 8.4
	NH_4^+	13.9 ± 9.8	19.6 ± 10.3	10.3 ± 7.5
	TNH_x	25.7 ± 14.6	30.3 ± 15.1	22.8 ± 13.5
U-XY	NH_3	7.0 ± 4.3	5.7 ± 4.0	7.9 ± 4.3
	NH_4^+	11.0 ± 7.7	15.4 ± 7.6	8.3 ± 6.5
	TNH_x	17.6 ± 9.8	20.6 ± 10.1	15.7 ± 9.2
R-AY	NH_3	19.0 ± 8.4	17.9 ± 8.3	19.7 ± 8.4
	NH_4^+	19.3 ± 12.9	26.4 ± 13.7	15.0 ± 10.3
	TNH_x	36.6 ± 18.2	41.7 ± 20.4	33.4 ± 16.0
R-XX	NH_3	21.7 ± 10.2	18.1 ± 9.3	23.8 ± 10.1
	NH_4^+	15.9 ± 10.4	20.6 ± 11.0	13.0 ± 8.8
	TNH_x	34.9 ± 17.0	35.1 ± 18.8	34.8 ± 15.8
R-PY	NH_3	19.8 ± 9.4	16.8 ± 8.1	21.7 ± 9.6
	NH_4^+	17.4 ± 11.8	25.3 ± 12.6	12.4 ± 8.0
	TNH_x	35.2 ± 17.8	39.4 ± 19.8	32.6 ± 15.7
R-JZ	NH_3	25.3 ± 11.5	24.1 ± 11.5	25.9 ± 11.4
	NH_4^+	17.3 ± 11.3	22.7 ± 11.6	14.2 ± 9.9
	TNH_x	40.8 ± 20.1	42.9 ± 22.8	33.5 ± 18.2
R-SQ	NH_3	15.0 ± 7.9	10.3 ± 5.2	17.7 ± 7.9
	NH_4^+	13.4 ± 8.5	18.9 ± 8.6	10.3 ± 6.7
	TNH_x	26.3 ± 13.2	25.5 ± 14.0	26.8 ± 12.7
R-NY	NH_3	5.5 ± 3.1	4.3 ± 2.7	6.2 ± 3.2
	NH_4^+	10.2 ± 6.9	13.3 ± 7.2	8.4 ± 6.1
	TNH_x	14.8 ± 8.5	16.0 ± 9.5	14.1 ± 7.8

698